

SparseAlign: A Fully Sparse Framework for Cooperative Object Detection

Yunshuang Yuan¹ Yan Xia^{2,3†} Daniel Cremers^{2,3} Monika Sester¹

¹Leibniz University Hannover ²Technical University of Munich ³Munich Center for Machine Learning (MCML)
 {yunshuang.yuan, monika.sester}@ikg.uni-hannover.de {yan.xia, cremers}@tum.de

Abstract

Cooperative perception can increase the view field and decrease the occlusion of an ego vehicle, hence improving the perception performance and safety of autonomous driving. Despite the success of previous works on cooperative object detection, they mostly operate on dense Bird’s Eye View (BEV) feature maps, which are computationally demanding and can hardly be extended to long-range detection problems. More efficient fully sparse frameworks are rarely explored. In this work, we design a fully sparse framework, *SparseAlign*, with three key features: an enhanced sparse 3D backbone, a query-based temporal context learning module, and a robust detection head specially tailored for sparse features. Extensive experimental results on both *OPV2V* and *DairV2X* datasets show that our framework, despite its sparsity, outperforms the state of the art with less communication bandwidth requirements. In addition, experiments on the *OPV2Vt* and *DairV2Xt* datasets for time-aligned cooperative object detection also show a significant performance gain compared to the baseline works.

1. Introduction

Cooperative Perception (CP) for autonomous driving has gained significant attention due to its potential to enhance road safety. Sharing Collective Perception Messages (CPMs) among Intelligent (traffic) Agents (IAs) in the vehicular network effectively reduces occlusions and expands the field of view, improving perception performance. In many recent works [1, 16, 24, 29, 35, 41, 42], CP has proven to be effective for different tasks, such as cooperative object detection [1, 24, 29, 41], Bird’s Eye View (BEV) semantic segmentation [19, 42], and 3D occupancy semantic segmentation [22]. In this work, we focus on LiDAR-based cooperative vehicle detection.

Training a cooperative 3D object detector is computationally demanding as it needs to process data from multiple vehicles, especially when the model is built to di-

[†]Corresponding author.

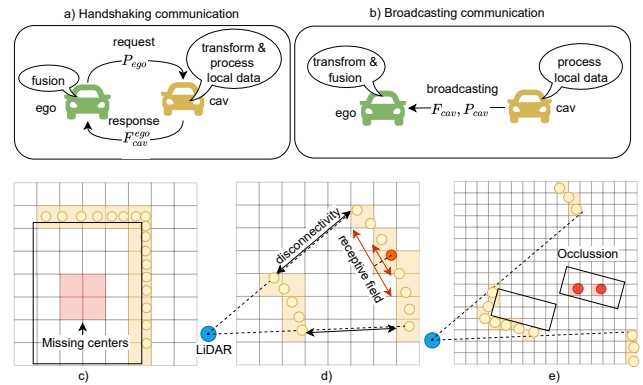


Figure 1. a,b) Communication strategies for cooperative object detection. c-e) Issues of sparse convolutional backbone networks. c) Center Feature Missing (CFM). d,e) Isolated Convolution Field (ICF) caused by ring disconnectivity and occlusion.

gest sequential data from several subsequent frames to learn the temporal context. Following Fcooper [1], recent works [6, 11, 28–30, 33, 35] encode the 3D point cloud into dense BEV feature maps for further processing, sharing, and fusion. However, the computational cost of this pipeline increases quadratically with the perception range. Although cooperation among IAs can improve long-range detection performance, the IAs are normally not in the best positions to optimize the performance gain. The long-range detection performance of the local detector directly influences the overall performance. Besides, sharing the BEV feature maps among IAs requires extensive communication resources. Instead, the sparse operations leverage the sparsity of point clouds and have only linear computational complexity relative to the number of points. In addition, the output sparse features can be more efficient for sharing. It is therefore beneficial to perform cooperative object detection based on sparse operations only.

However, building a fully sparse framework to compete with the dense ones is non-trivial. The first unavoidable issue is **Center Feature Missing** [8] (CFM, shown in Fig. 1 c)). Due to the range view of on-board LiDARs, there are

usually no scan points in the vehicles’ center area. However, compared to the edge points, the center points have a better ability to represent the whole object. Lacking center points for learning, the sparse frameworks perform worse than the dense ones that directly learn the features for center points. The second issue is the poor connectivity between points scanned by different laser beams. As shown in Fig. 1 d), this disconnectivity issue in distant areas may lead to isolated voxel blobs; the receptive field only enlarges to the blob scale as the convolutional layers go deeper. The isolated voxel blobs never exchange information with each other, limiting the backbone’s capability of capturing global features. We call this issue **Isolated Convolution Field (ICF)**. It also happens in the occlusion areas as shown in Fig. 1 e): although the occluded vehicle has very few scan points (red), it is expected to be detected based on the neighboring vehicles and the clues in the previous frames. However, ICF introduces difficulties for these isolated points to aggregate information from neighbors and the global environment.

To overcome the above problems, we build a **Sparse UNet** backbone network *SUNet* with the **Coordinate-Expandable sparse Convolution (CEC)** implemented in the MinkowskiEngine [5] library. We apply CEC on $4\times$ and $8\times$ downsampled 3D voxels to increase the connectivity between ICFs. On the 2D BEV features, the CECs are used to expand the sparse coordinates, assuring the center features for all scanned vehicles. On top of SUNet, we build *TempAlign Module (TAM)* to learn the temporal context from the historical frames in a query-based [23, 40] manner, *PoseAlign Module (PAM)* to correct the relative pose errors between the cooperative and the ego agents, and *SpatialAlign Module (SAM)* to fuse the shared object queries based on the corrected poses. In addition, we propose the *CompassRose* encoding for the regression of BBox directions to further improve performance on both Cooperative Object Detection (COOD) and the Time-Aligned COOD [40] (TA-COOD) tasks.

To summarize, the main contributions of this work are:

- We investigate the issues of building a fully sparse network for LiDAR-based COOD and analyze how these issues impact the detection performance.
- We propose a novel fully sparse network, *SparseAlign*, via addressing the ICF and CFM problems of the sparse 3D backbone SUNet with CECs. Additionally, we introduce the SAM module, specifically tailored to ensure accurate fusion of sparse features.
- We assess the communication bandwidth and precision trade-offs of the different approaches, finding that our proposal reduces bandwidth consumption by up to 98%, compared to previous methods using dense BEV feature maps for LiDAR-based cooperative object detection.
- We conduct extensive experiments on OPV2V, DairV2X, OPV2Vt, and DairV2Xt benchmarks and show that the

proposed *SparseAlign* has a significant improvement over state-of-the-art methods.

2. Related Work

2.1. Cooperative Object Detection (COOD)

COOD frameworks are classified into sharing CPMs with raw data, intermediate features, and detections. Recent works [2, 24, 29, 38] have shown that intermediate feature sharing has the best performance due to its adjustable and learnable CPMs. We also use this strategy in our framework. In the perspective of communication, there are two strategies: *handshaking* and *broadcasting* as shown in Fig. 1 a) and b). With handshaking communication [11, 28–30, 33, 40, 42], the ego vehicle sends a request message that contains its pose to the cooperative IAs so that they can transform the local raw data to the ego coordinate system and then process their data to obtain the features for sharing. This simplifies the feature fusion process, as the features are directly learned in the goal coordinate system. In contrast, the *broadcasting* method [6, 17, 24, 37] directly processes the data in the local coordinate system and transmits it to other IAs. In the fusion stage, the ego vehicle must transform the cooperative features into the ego coordinate system and then conduct the fusion process. In comparison, *broadcasting* is more efficient as it does not require a prior communication agreement with the cooperative agents in highly dynamic driving scenarios where the communication partners change frequently.

Achieving COOD presents several challenges, including communication latency and bandwidth limitations, inaccurate IA poses, and sensor asynchrony. To reduce the **communication bandwidth** consumption, [1, 24, 29, 33] compress the learned BEV feature maps to fewer channels via convolution layers, while [13] utilizes the learned confidence map and [42] leverages the uncertainty map to select the most important information for sharing. Instead, [41] employs the two-stage detector PVRCNN [20] and shares the 3D keypoint features from the second stage. To be more compact, [4, 9, 40] share the object query features [23] which are highly flexible to blend all relevant information, such as scanning time and IA pose, about an object into one unique feature vector. In this work, we also leverage the object query features to learn the temporal and spatial context of the object. **Pose errors** can dramatically deteriorate the detection results [24]. To this end, [39, 41] leverage the predicted Bounding Boxes (BBoxes) and select semantically classified keypoints to align the relative pose between the ego and the cooperative vehicles. Instead, [17] solely uses the BBoxes for pose alignment via the *Pose Graph Optimization (PGO)*. However, these methods require the initial pose errors to be small to find the correct object matching in the first step and then iterate many times, or use the PGO

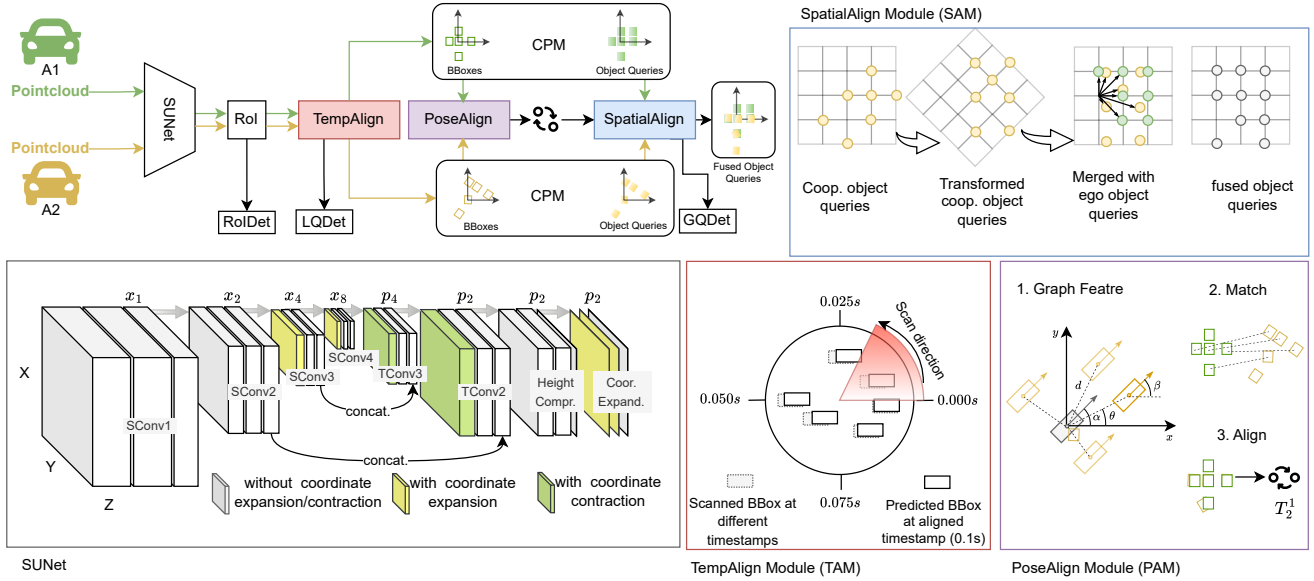


Figure 2. Overview of SparseAlign framework

to refine the result. In this paper, we propose to learn pose-agnostic neighborhood graph features to accurately find the correct matching and then use PGO to refine it. **Communication delay** can cause that data arriving at the ego agent is outdated. To compensate for this delay, [36, 37] add the first-order derivatives of the BEV feature map to the original feature map to obtain the updated feature map that is aligned to the ego timestamp; [15] employs the LSTM [12] structure on the BEV feature maps to adjust the features to be aligned. Differently, [40] embeds the observation timestamps as well as the temporal context from historical frames into the object queries so that they are time- and motion-aware and capable of predicting the status at any given future timestamp, achieving the time-delay compensation. Different to [15, 36, 37] that compensate the feature maps, [40] leverages the point-wise timestamp of the point clouds to learn the accurate temporal context, hence is also able to cope with **sensor asynchrony** issues. Therefore, we adopt the query-based strategy for time-related compensation.

2.2. 3D Backbones

To extract point cloud features, most previous works [16, 17, 24, 29, 33, 37, 41] for COOD either use dense 3D [25, 44], dense 2D [14, 32] or semi-sparse [21, 26, 31, 43] backbones that first encode the point cloud with 3D sparse convolution and then apply dense 2D convolutions for further processing. In contrast, [40, 42] employ the MinkUnet [5] to extract point cloud features. Despite its efficiency, the MinkUnet backbone struggles with long-range detection, occlusions and large objects, because of CFM and ICF problems. [8] proposed center voting for each scanned ob-

ject points to solve CFM issue and [3] reveals that further down-sampling the voxel features to lower resolutions can increase the receptive field and refine the large object detection. Instead of shifting the feature locations as [8] to accurately locate object queries or adding additional layers as [3], we build a backbone that solves both CFM and ICF issues by modifying MinkUnet with CEC layers.

3. Method

3.1. Task formalization

In this work, we solve the LiDAR-based cooperative object detection task considering unavoidable challenges in reality: communication delay, sensor asynchrony, and localization errors. For this scenario, we assume there are N IAs, including one ego agent A_1 and $N - 1$ cooperative agents. These agents are sharing CPMs with each other in a broadcasting manner, as shown in Fig. 1b). Specifically, in the i -th frame, A_1 receives the CPMs $M = \{(m_j, t_j) | j \in \{1, \dots, N - 1\}\}$ from the cooperative agents, where m_j and t_j are the CPM and the corresponding timestamp from the j -th agent. We aim to optimize the object detection results based on the point clouds captured so far ($t \leq t_i$) at A_1 and the received messages M . We model and evaluate both the COOD and TA-COOD tasks from the perspective of an ego agent. The key difference between COOD and TA-COOD lies in the GT BBoxes. As illustrated in Fig. 2, TAM, COOD GT BBoxes (dashed lines) align with the sequentially captured LiDAR points, whereas TA-COOD GT BBoxes (solid lines) are referenced to a global timestamp t_g . This distinction requires the model to accurately predict

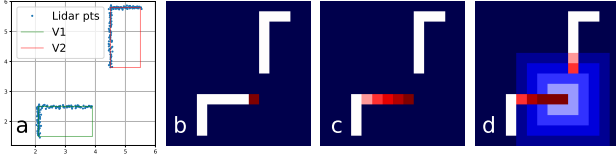


Figure 3. Receptive field (RF) after 4 sparse convolutions (convs). a. LiDAR points; b. Spare pixels (white) with a conv center point (red); c. RF coverage of 4 normal sparse convs (red); d. RF coverage of 4 CECs (red+light blue, darkest blue is background).

BBox locations at t_g . While COOD relies solely on point cloud geometry for location prediction, TA-COOD leverages temporal context to enhance accuracy at t_g and also enables the model to handle location errors due to communication latency.

3.2. Framework overview

We build an efficient fully sparse framework *SparseAlign*, as shown in Fig. 2, to process sequential point clouds from multiple agents. All agents share the same network weights. The input at time t_i is the point cloud of the ego agent PC_{t_i} and of the cooperative agents PC_{t_j} . Note that $t_j < t_i$ when communication latency exists. All point clouds are processed by the backbone SUNet to extract the point cloud features. The Region of Interest (RoI) module then selects the most interesting features as the object queries. For simplicity, we define object queries as $Q^* = \{(F_i^*, x_i^*, y_i^*) | i \in \{1, \dots, N^*\}\}$, where $*$ represents the query set name, F is the features, and x, y are the coordinates of the corresponding i -th query. With selected queries, the TempAlign Module (TAM) can efficiently align the query features to the globally aligned timestamp t so that errors introduced by communication delay and sensor asynchrony are compensated. The updated query features and the detections from the Local Query Detection head (LQDet) are then shared as CPMs. The PoseAlign Module (PAM) then uses the detected BBoxes to correct the relative poses between the cooperative and the ego agent and the SpatialAlign Module (SAM) fuses the received cooperative features into the ego coordinate system based on the corrected transformation T_c^e from cooperative to ego coordinates.

3.3. Backbone: Sparse UNet (SUNet)

Processing data from multiple IAs for cooperative perception is computationally demanding. To improve efficiency, we use a fully sparse 3D UNet, similar to MinkUnet[5], to construct the SUNet (Fig. 2 bottom left). However, the fully sparse convolutions used in such networks suffer from the ICF issue. As shown in Fig. 3, the receptive field (RF) of (c) standard sparse convolutions only covers LiDAR points from a single vehicle. In contrast, the RF of (d) the CEC layers extends to the points of a neighboring vehicle, enabling learning within a larger spatial context. Therefore,

we use 3D CECs in the sparse convolution (SConv) block 3 and 4. Correspondingly, we contract the coordinates in the transposed sparse convolution (TConv) block 3 and 2. In this way, the output of the TConv blocks $p4$ and $p2$ can match the coordinates in stride $x2$ and $x4$ for the concatenation. In addition, it learns better global features without voxel number soaring in the subsequent layers and maintains efficiency. Against the CFM issue, we use 2D CECs on the 2D BEV sparse features (Fig. 2 SUNet:Coor. Expand.) to expand the coordinates to ensure their coverage over the object centers.

3.4. Alignment modules

TempAlign Module (TAM). The TAM aims to learn the temporal context relative to the previous frames to achieve two goals: improve object detection performance by looking for clues in the history and compensate for the object displacement error introduced by asynchronous scanning time (Fig. 2, TAM). We achieve the second goal by predicting the BBoxes at the globally aligned timestamp so that the BBoxes shared for PAM are synchronized. Then PAM only needs to deal with the object displacement caused by localization errors. Technically, the TAM follows [40], for efficiency, by removing the global cross-attention module which learns the global BEV features. We only use a memory queue and a hybrid attention module. The memory queue stores the top $k = 256$ object queries from previous $L = 4$ data frames so that the attention module can allow the interaction between object queries in the current frame and the historical frames. In this way, the object queries learn the temporal context from the sequential data and are able to make predictions for the future state.

PoseAlign Module (PAM). Given the detected BBoxes \mathbf{B}_i and \mathbf{B}_j , respectively, from the perspective of the agent A_i and A_j in the same scene, humans can easily find the correspondences between \mathbf{B}_i and \mathbf{B}_j based on the geometric relationships. Practically, we model the features of these geometric relationships by embedding the neighborhood geometry of each BBox into deep features and then match these features of \mathbf{B}_i and \mathbf{B}_j with the Hungarian algorithm. For each BBox b in a BBox set \mathbf{B} , we select the nearest $k = 8$ neighbors to embed its neighborhood features. As shown in Fig. 2, PAM: *1.Graph Feature*, the orientation angles of the BBox are α and β for b and its neighbor, respectively. We embed the relative orientation with $\nu_a = [\sin(\beta - \alpha); \cos(\beta - \alpha)]^1$. Similarly, the relative edge direction is embedded as $\epsilon_a = [\sin(\theta - \alpha); \cos(\theta - \alpha)]$. In addition, the dimension $\nu_{dim} = [l, w, h]$ of the neighbor BBox, and the Euclidean distance between b and its neighbors $\epsilon_d = d$, are also embedded into the feature. Note that $\epsilon_d, \epsilon_a, \nu_a$ are all relative features between two BBoxes that are pose-agnostic, leading to robust pose alignment without

¹ $[\cdot; \cdot]$: concatenation

dependency on the magnitude of initial pose errors. These features are then concatenated and embedded into high-dimensional features by a *linear* layer with ReLU activation ($\mathbb{R}^5 \rightarrow \mathbb{R}^{d_{emb}}$):

$$f_{nbr} = \text{linear}([\epsilon_d; \epsilon_a; \nu_a; \nu_{dim}]) \quad (1)$$

Assembling the features relative to all neighbors, we summarize the neighborhood feature $F_{nbr} \in \mathbb{R}^{k \times d_{emb}}$ by a multi-head self-attention module *attn* followed by a *linear* layer operated on the *mean* and *max* of the *attn* outcome, resulting in the feature $F_{nbr} \in \mathbb{R}^{d_{emb}}$:

$$F_{nbr} = \text{attn}(F_{nbr}) \quad (2)$$

$$F_{nbr} = \text{linear}([\text{mean}(F_{nbr}); \text{max}(F_{nbr})]) \quad (3)$$

By calculating the Euclidean distance between the learned neighborhood feature F_{nbr} of the BBox in \mathbf{B}_i and \mathbf{B}_j , we construct the cost matrix for the linear sum assignment to find the best *Match* (Fig. 2, PAM: 2.*Match*) between these two BBox sets. However, an object in \mathbf{B}_i does not always have a projection in \mathbf{B}_j and vice versa. Thus, we reject the wrong matches that have large distances. Based on the PAM: 2.*Match* result, the relative pose transformation between A_i and A_j can be recovered, completing the PAM: 3.*Align* step. Additionally, we use pose graph optimization to refine the alignment by leveraging loop closure among multiple cooperative agent poses following [17].

SpatialAlign Module (SAM). To align the cooperative query features Q^c with the ego query features Q^e , there are two issues to be resolved. First, the features F^c are learned in the cooperative coordinate system and must be adapted to the ego coordinate system. We achieve this using a multilayer perceptron (*MLP*) as described in Eq. (4) where $F^R \in \mathbb{R}^{N \times 9}$ is the flattened and repeated rotation matrix $R \in \mathbb{R}^{3 \times 3}$.

$$F^c = \text{MLP}([F^c; F^R]) \quad (4)$$

Second, after rotation with R , the coordinates of Q^c (Fig. 2, SAM, yellow points) do not perfectly align to the discretized grid in the ego coordinate system. Thus, we merge Q^c into the nearest points of this grid. The locations of the fused output object query points Q^{ts} are shown with gray points. For each point in Q^{ts} , we summarize the features of its $k = 8$ nearest neighbors (Fig. 2, SAM: black arrows) in query set $Q^\cup = Q^c \cup Q^e$ to obtain the fused features F^{ts} . Mathematically, it reads as

$$F_{ij} = \text{mlp}([F_j^\cup; \text{linear}([x_i^{ts} - x_j^\cup, y_i^{ts} - y_j^\cup])]) \quad (5)$$

$$F_i^{ts} = \{F_{ij} | j \in \{1, \dots, k\}\} \quad (6)$$

$$F_i^{ts} = \text{max}_j(F_i^{ts}) + \text{mean}_j(F_i^{ts}) \quad (7)$$

where i is the query index of Q^{ts} and j is the neighbor index of the i -th query.

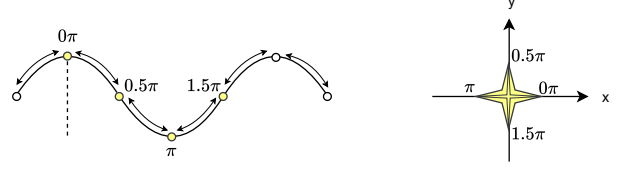


Figure 4. CompassRose encoding

3.5. Detection Heads

To train *SparseAlign*, we follow [40] to attach a center-based object detection head to each of the RoI, TAM and SAM to learn query features. These heads are notated as *RoIDet*, *LQDet* and *GQDet*, respectively. They share the same target-encoding method. We use *Focal* loss to classify fore- and background object queries; all query points inside the ground-truth BBoxes are positive, and those outside are negative. *Smooth L1* loss is used for regressing $[dx, dy, dz, l, w, h, \mathcal{B}_{dir}, \mathcal{B}_{scr}]$, where l, w, h are the dimensions of BBoxes and dx, dy, dz are coordinate offsets between the query points and the center of ground-truth BBoxes. $\mathcal{B}_{dir}, \mathcal{B}_{scr}$ are the novel *CompassRose* encoding (Fig. 4) of the ground truth orientation r_g with respect to four anchor angles $\mathbf{r}_a = [0, 0.5\pi, \pi, 1.5\pi]$. It reads as

$$\mathcal{B}_{dir} = [\cos r_g - \cos \mathbf{r}_a, \sin r_g - \sin \mathbf{r}_a] \quad (8)$$

$$\begin{aligned} \mathcal{B}_{scr} &= [s_0, s_{0.5\pi}, s_\pi, s_{1.5\pi}] \quad (9) \\ &= \mathbf{1} - \arccos(\cos \mathbf{r}_a \cdot \cos r_g + \sin \mathbf{r}_a \cdot \sin r_g) / \pi \end{aligned}$$

Take the encoded *sine* wave (Fig. 4 left) as an example, the four anchor angles (yellow points) ensure that at least one anchor can reach the target angle monotonically, simplifying the regression process.

3.6. Data augmentation

In addition to geometric augmentation, which includes randomly flipping the input point cloud along the x- or y-axis and rotating it around the z-axis, we apply Free Space Augmentation (FSA) [42]. FSA enhances the point cloud by adding auxiliary points along LiDAR scanning rays, representing empty spaces where no objects are present. This augmentation helps mitigate the ICF problem in distant regions, where observation points are extremely sparse. For more details, refer to *supplementary B*.

4. Experiment

Datasets. We evaluate *SparseAlign* on OPV2V[29] and DairV2X[35] datasets for COOD and their variant datasets OPV2Vt[40] and DairV2Xt[40] for TA-COOD. OPV2V is a synthetic dataset created in different driving scenarios of CARLA [7] simulator. Following [29], the detection range is set to $x \in [-140, 140]m, y \in [-40, 40]m$.

Method	BW(Mb) ↓	AP0.5 ↑	AP0.7↑
Fcooper[1]	72.08	0.887	0.790
V2VNet[24]	72.08	0.917	0.822
FPVRCNN[41]	0.24	0.873	0.820
OPV2V[29]	126.8	0.905	0.815
CoAlign[17]	72.08	0.902	0.833
CoBEVT[19]	72.08	0.913	0.861
V2VAM[16]	72.08	0.916	0.850
V2VFormer++[34] ^{L+C}	72.08	0.935	0.895
SparseAlign (ours)	< 1.3	<u>0.930</u>	<u>0.892</u>

Table 1. COOD Average Precision on OPV2V dataset.

2

Method	OPV2Vt		DairV2Xt	
	AP0.5↑	AP0.7↑	AP0.5↑	AP0.7↑
Fcooper[1]+SA	0.763	0.553	0.597	0.282
FPVRCNN[43]+SA	0.640	0.474	0.598	0.307
OPV2V[29]+SA	<u>0.881</u>	0.787	0.702	0.366
StreamLTS[40]	0.853	0.721	0.640	0.404
StreamLTS[40]+SA	0.850	<u>0.790</u>	<u>0.757</u>	<u>0.497</u>
SparseAlign (full)	0.893	0.818	0.796	0.548

Table 3. TA-COOD Average Precision on OPV2Vt and DairV2Xt

DairV2X is a real dataset containing one vehicle- and one infrastructure-side sensor suit. The detection range is set to $x \in [-100, 100]m, y \in [-40, 40]m$. OPV2Vt is generated by interpolating OPV2V data frames into sub-frames and replaying them to mimic the sensor asynchrony and the rolling shutter problem of LiDARs. The GT BBoxes of this dataset are aligned to the global timestamp, the LiDAR scan ending time of each frame. DairV2Xt follows the same idea. The detection range of OPV2Vt and DairV2Xt is set the same as OPV2V and DairV2X.

Implementation details. All models are trained on a single GTX-4090 and an Intel i7-8700 CPU for 50 epochs (about 35 hours) with the Adam optimizer and batch size two. The learning rate is set to $2e - 4$ with a warm-up stage of 4000 iterations. The random rotation angle is set to the range $[-90^\circ, 90^\circ]$. For models incorporating the TAM, we load four sequential frames of data during training and calculate losses solely for the last frame. To reduce GPU memory consumption, we enable gradient calculations only for data from a single ego agent and one cooperative agent. For details on efficient gradient scheduling, refer to *supplementary D*. To ensure that the model generalizes well to the significant time latency introduced by communication, we load data from cooperative vehicles with a random latency ranging from 0 to 200 ms relative to the ego vehicles.

²The results reported in this table use frame-wise local score sorting for AP, same to the official benchmark. Other results use global sorting.

Method	BW(Mb) ↓	AP0.5 ↑	AP0.7↑
Fcooper[1]	48.8	0.734	0.559
V2VNet[24]	48.8	0.664	0.402
FPVRCNN[41]	0.24	0.665	0.505
V2XViT[28]	48.8	0.704	0.531
DiscoNet[19]	48.8	0.736	0.583
OPV2V[29]	97.6	0.733	0.553
CoAlign[17]	48.8	0.746	0.604
DI-V2X[27]	48.8	<u>0.788</u>	<u>0.662</u>
SparseAlign (ours)	< 1.3	0.845	0.685

Table 2. COOD Average Precision on DairV2X dataset.

5. Results

5.1. Comparison to the state-of-the-art

Tab. 1 presents the COOD results on the OPV2V dataset. All methods use only LiDAR data, except for *V2VFormer++* (denoted by L+C), which incorporates both LiDAR and camera data. Compared to the state-of-the-art, our *SparseAlign* achieves the best performance in LiDAR-based COOD, approaching the results of *V2VFormer++*, which benefits from LiDAR-Camera fusion. Tab. 2 shows the results on the DairV2X dataset. Here, *SparseAlign* outperforms other methods by a large margin, achieving a 2.3% improvement in AP at the IoU threshold of 0.7 and a 5.7% improvement at the IoU threshold of 0.5. This is mainly due to the enhanced temporal and global reasoning ability of our model for detecting distant and large objects. Compared to other methods that rely on dense BEV feature maps, *SparseAlign* consumes the least communication bandwidth (BW) of less than 1.3MB (without compression) thanks to the efficient query-based operations.

For the results of the more challenging TA-COOD task shown in Tab. 3, our *SparseAlign* outperforms *StreamLTS* by a great margin. By applying our three alignment modules (*StreamLTS+SA*), the performance of *StreamLTS* is also improved. In addition, we compare our framework to *Fcooper*, *FPVRCNN* and *OPV2V* method by attaching the three alignment modules to them to achieve TA-COOD. All show worse performance than the full *SparseAlign* because of worse 3D backbone or the RoI selection.

The qualitative results and the additional comparison to methods, such as *TransIFF*[4], on the 3D AP metric are given in the *supplementary A* and *E*, respectively.

5.2. Ablation study

We conduct an ablation study on the 3D backbone, TAM, and SAM (PAM is discussed separately in Sec. 5.4). Among these components, the spatial fusion module plays a crucial role in multi-agent feature fusion. Without SAM, the module performs the worst, as evidenced by the first row

CEC 2D	CEC 3D	TAM	SAM	OPV2V		DairV2X	
				AP0.5	AP0.7	AP0.5	AP0.7
✓	✓	✓		0.847	0.756	0.671	0.528
✓	✓	✓	QST	0.888	0.869	0.749	0.622
			✓	0.924	0.885	0.773	0.638
✓			✓	0.940	0.901	0.796	0.662
✓	✓		✓	0.950	0.914	0.813	0.682
✓	✓	✓	✓	0.951	0.929	0.845	0.685

Table 4. Ablation study on 2D and 3D CEC layers, TAM and SAM. QST: use QUEST [9] spatial fusion instead of SAM.

Dataset	OPV2Vt						DairV2Xt					
	0ms		100ms		200ms		0ms		100ms		200ms	
	AP	IoU	AP	IoU	AP	IoU	AP	IoU	AP	IoU	AP	IoU
SteamLTS [40]	0.853	0.721	0.816	0.680	0.787	0.647	0.642	0.404	0.613	0.379	0.590	0.364
SA no TAM	<u>0.890</u>	0.802	0.856	0.471	0.631	0.209	0.720	0.457	0.672	0.393	0.635	0.350
SA no PT	0.835	0.615	0.831	0.625	0.815	0.581	0.760	0.469	0.737	0.459	0.722	0.449
SA no TL	0.885	0.843	0.862	0.619	0.723	0.279	<u>0.793</u>	<u>0.534</u>	0.749	0.474	0.698	0.423
SA no FSA	0.881	0.816	<u>0.875</u>	0.795	<u>0.857</u>	<u>0.762</u>	0.769	0.508	<u>0.755</u>	<u>0.502</u>	<u>0.740</u>	<u>0.496</u>
SparseAlign (SA)	0.893	<u>0.818</u>	0.885	0.795	0.867	0.765	0.796	0.548	0.786	0.543	0.772	0.532

Table 6. AP of TA-COOD with communication latency. PT: Point-wise Timestamps, TL: Train Latency, FSA: Free Space Augmentation.

of Tab. 4. When using QUEST [9] spatial fusion, which aligns only rotation (Eq. (4)) without correcting spatial displacement (Eqs. (5) to (7)), the AP scores remain significantly lower than those obtained with SAM. Incorporating SAM improves performance, and we further enhance it by gradually replacing standard sparse convolutional layers with CEC layers. Finally, TAM further boosts AP scores by leveraging temporal information from historical frames.

In Tab. 5, we compare CompassRose encoding with three methods: directly regress the ground-truth angle (*gt-angle*), second-style [31] encoding (*second*), and the sine-cosine encoding (*sin_cos*). For simplicity, we use the configurations in the third row of Tab. 4 for the comparison. The results show that CompassRose performs the best.

5.3. Communication latency and sensor asynchrony

Tab. 6 shows the results of TA-COOD on the OPV2Vt and the DairV2Xt dataset. Our proposed *SparseAlign* demonstrates a significant improvement over the baseline framework, *StreamLTS* [40]. Specifically, the AP at an IoU threshold of 0.7 increased 9.7% on the OPV2Vt dataset and 14.4% on the DairV2Xt dataset. As the communication latency increases to 200ms, the AP at IoU 0.5 of our *SparseAlign* only dropped 2.6% while the baseline work has lost 6.6% of its accuracy. This reveals that our framework is more robust against communication latency. To investigate modules or configurations that are making an effect on this robustness, we conducted an ablation study by removing the TAM, Point-wise Timestamps (TP), Training

Dir. Enc.	OPV2V		DairV2X	
	AP0.5	AP0.7	AP0.5	AP0.7
<i>gt-angle</i>	0.871	0.768	0.620	0.427
<i>second</i>	0.908	0.874	0.743	0.590
<i>sin_cos</i>	0.915	0.881	0.748	0.603
<i>compass</i>	0.924	0.885	0.773	0.638

Table 5. Comparison on BBox angle encoding methods: offset to ground-truth angle (*gt-angle*), second-style (*second*), sine-cosine offsets (*sin_cos*) and compass rose (*compass*).

Latency (TL, communication latency during training) and Free Space Augmentation (FSA), respectively.

Without the TAM, the performance noticeably declines as latency increases, despite achieving comparable results to the full *SparseAlign* model at 0 ms latency. A similar effect is observed when the full SA model is trained without exposure to data with communication latency (SA without TL). Remarkably, without TL, the model outperforms the full *SparseAlign* model in terms of AP at an IoU threshold of 0.7 on the OPV2Vt dataset (0.843 against 0.818). This is because the model focuses more on predicting BBoxes within the same frame, where only minimal latency is introduced by asynchronous sensors.

Without PT, the model performs much worse than the full *SparseAlign*, showing the importance of fine-grained point-wise timestamps in the point clouds for the model to compensate for the errors introduced by sensor asynchrony and capture the accurate temporal context for prediction. Finally, the ablation study on the FSA module also shows a positive influence on the performance. For example, AP at the IoU of 0.7 increased by 4% on DairV2Xt by utilizing the FSA (See *supplementary D* for visual comparison).

5.4. Localization errors

Fig. 5 shows the performance of *SparseAlign* against different localization errors. We add random errors to the poses of both ego (T_e) and cooperative (T_c) vehicles. The translation errors x_ϵ, y_ϵ along the x - and y -axis and the rotation error r_ϵ around the z -axis are all assumed to be normally distributed

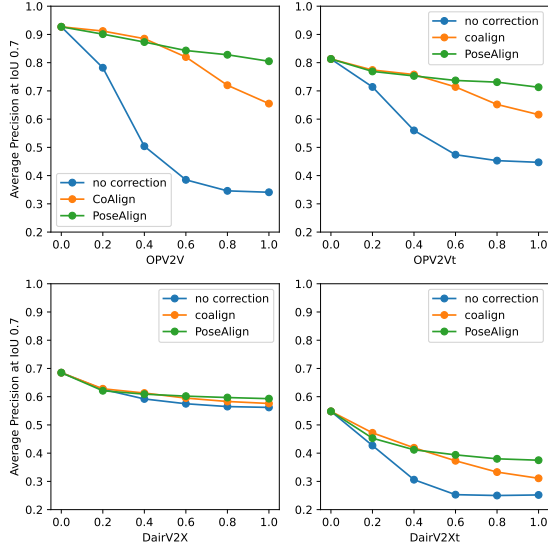


Figure 5. AP at IoU threshold of 0.7 with translation errors ranging from 0m to 1m along x- and y-axis, and rotation errors from 0° to 1.0° (horizontal axis) for the different datasets.

with $\mathcal{N}(0, 1) \cdot \epsilon$, where $\epsilon \in [0, 1]$ is the error scaling factor. We report the results by gradually increasing ϵ with a step size of 0.2. Note that the translation and rotation errors exist in the poses of both the ego and the cooperative vehicle; the resulting relative translation error of the transformation $T_c^e = \text{inverse}(T_e) \cdot T_c$ from cooperative to ego coordinate system will be amplified as the rotation error increases. Our *PAM* is specially designed to mitigate the influence of large relative transformation errors.

Our proposed *PAM* and the baseline method *CoAlign* [17] both significantly reduce the impact of pose errors on AP performance compared to the configuration lacking any correction module. In addition, our method demonstrates greater robustness against large errors. For instance, on the OPV2V dataset, the AP for *CoAlign* decreased by approximately 27% at the error of 1.0m, 1.0m, 1.0° , whereas *PAM* experienced only a 12% drop. This validates the efficacy of our design, which relies on the pose-agnostic relative neighborhood geometries to match the detected BBoxes of the ego and the cooperative IAs. Note that the DairV2X dataset exhibits smaller changes in AP as localization errors increase, because the pose parameters are not well calibrated. In contrast, [40] refined the poses of DairV2X for generating the DairV2Xt dataset, making the better-calibrated DairV2Xt more sensitive to newly introduced errors.

5.5. CPM sizes

Our framework significantly reduces communication bandwidth without relying on computationally intensive dense

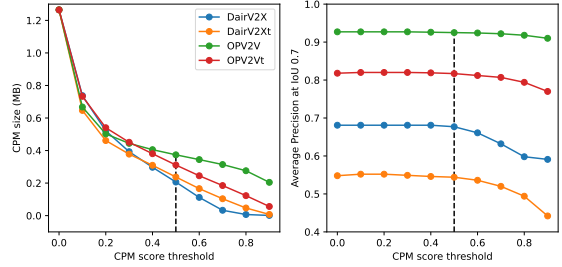


Figure 6. CPM sizes with different information selection scores. Object query features with detection scores larger than the threshold (x-axis) are shared as CPMs.

feature maps, unlike state-of-the-art methods. This efficiency is achieved by selecting only the top $K = 1024$ object queries for further processing. In addition to this intrinsic reduction, the size of the CPMs can be further minimized through score-based selection. Specifically, we employ the query-based detection scores from the LQDet head to identify and share only the most critical queries. As Fig. 6 shows, using a CPM score threshold below 0.5 does not lead to a noticeable degradation in performance across all datasets. Remarkably, at a threshold score of 0.5, the average size of the CPMs is reduced to less than 400 KB on all datasets. The final CPM sizes after selection are influenced by the driving scenes. Specifically, scenes with more vehicles tend to have larger CPM sizes. Consequently, the OPV2V and OPV2Vt datasets, which contain more vehicles in their scenes, result in larger CPM sizes compared to the DairV2X and DairV2Xt datasets.

6. Conclusion

In this paper, we proposed *SparseAlign*, a fully sparse framework for cooperative object detection (COOD). With our novel 3D backbone network SUNet, the CompassRose encoding of detection head, the temporal and spatial fusion module TAM and SAM, *SparseAlign* significantly outperforms state-of-the-art methods on the OPV2V and DairV2X datasets for COOD, as well as on their variants OPV2Vt and DairV2Xt for time-aligned COOD (TA-COOD), achieving this with very low communication bandwidth. Additionally, our proposed pose alignment module *PAM* demonstrates improved robustness to large localization errors compared to the baseline method *CoAlign*. Nevertheless, when the pose errors are large, a drop of about 10% in APs persists even with pose correction. In future work, we therefore plan to explore more robust methods, *e.g.* leveraging sub-graph detection, to further enhance the pose alignment accuracy. Additionally, more application scenarios, such as roadside cooperative detection benchmarks HoloVIC[18], RCooper[10] and TUMTraF[45], could also be explored.

References

- [1] Qi Chen. F-cooper: feature based cooperative perception for autonomous vehicle edge computing system using 3d point clouds. *Proceedings of the 4th ACM/IEEE Symposium on Edge Computing*, 2019. 1, 2, 6
- [2] Qi Chen, Sihai Tang, Qing Yang, and Song Fu. Cooper: Cooperative perception for connected autonomous vehicles based on 3d point clouds. *2019 IEEE 39th International Conference on Distributed Computing Systems (ICDCS)*, pages 514–524, 2019. 2
- [3] Yukang Chen, Jianhui Liu, Xiangyu Zhang, Xiaojuan Qi, and Jiaya Jia. Voxelnxt: Fully sparse voxelnet for 3d object detection and tracking. *2023 IEEE/CVF Conference on Computer Vision and Pattern Recognition (CVPR)*, pages 21674–21683, 2023. 3
- [4] Ziming Chen, Yifeng Shi, and Jinrang Jia. TransIFF: An instance-level feature fusion framework for vehicle-infrastructure cooperative 3d detection with transformers. In *2023 IEEE/CVF International Conference on Computer Vision (ICCV)*, pages 18159–18168, 2023. 2, 6, 3
- [5] Christopher Bongsoo Choy, JunYoung Gwak, and Silvio Savarese. 4d spatio-temporal convnets: Minkowski convolutional neural networks. *2019 IEEE/CVF Conference on Computer Vision and Pattern Recognition (CVPR)*, pages 3070–3079, 2019. 2, 3, 4
- [6] Jiaxun Cui, Hang Qiu, Dian Chen, Peter Stone, and Yuke Zhu. Coopernaut: End-to-end driving with cooperative perception for networked vehicles. In *IEEE/CVF Conference on Computer Vision and Pattern Recognition (CVPR)*, page 17252–17262, 2022. 1, 2
- [7] Alexey Dosovitskiy, Geman Ros, Felipe Codevilla, Antonio Lopez, and Vladlen Koltun. CARLA: An open urban driving simulator. In *Proceedings of the 1st Annual Conference on Robot Learning*, pages 1–16, 2017. 5
- [8] Lue Fan, Feng Wang, Naiyan Wang, and Zhaoxiang Zhang. Fully Sparse 3D Object Detection. In *NeurIPS*, 2022. 1, 3
- [9] Siqi Fan, Haibao Yu, Wenxian Yang, Jirui Yuan, and Zaiqing Nie. Quest: Query stream for practical cooperative perception. In *IEEE International Conference on Robotics and Automation (ICRA)*, 2024. 2, 7
- [10] Ruiyang Hao, Siqi Fan, Yingru Dai, Zhenlin Zhang, Chenxi Li, Yuntian Wang, Haibao Yu, Wenxian Yang, Yuan Jirui, and Zaiqing Nie. Rcooper: A real-world large-scale dataset for roadside cooperative perception. In *Proceedings of the IEEE/CVF Conference on Computer Vision and Pattern Recognition (CVPR)*, pages 22347–22357, 2024. 8
- [11] Caizhen He, Hai Wang, Long Chen, Tong Luo, and Yingfeng Cai. V2x-ahd: vehicle-to-everything cooperation perception via asymmetric heterogenous distillation network. *arXiv*, arXiv:2310.06603, 2023. arXiv:2310.06603 [cs]. 1, 2
- [12] Sepp Hochreiter and Jürgen Schmidhuber. Long short-term memory. *Neural Computation*, 9(8):1735–1780, 1997. 3
- [13] Yue Hu, Shaoheng Fang, Zixing Lei, Yiqi Zhong, and Siheng Chen. Where2comm: Communication-efficient collaborative perception via spatial confidence maps. In *Thirty-sixth Conference on Neural Information Processing Systems (Neurips)*, 2022. 2
- [14] Alex H. Lang, Sourabh Vora, Holger Caesar, Lubing Zhou, Jiong Yang, and Oscar Beijbom. Pointpillars: Fast encoders for object detection from point clouds. *2019 IEEE/CVF Conference on Computer Vision and Pattern Recognition (CVPR)*, pages 12689–12697, 2018. 3
- [15] Zixing Lei, Shunli Ren, Yue Hu, Wenjun Zhang, and Siheng Chen. Latency-aware collaborative perception. In *Computer Vision – ECCV 2022*, page 316–332, 2022. 3
- [16] Jinlong Li, Runsheng Xu, Xinyu Liu, Jin Ma, Zicheng Chi, Jiaqi Ma, and Hongkai Yu. Learning for vehicle-to-vehicle cooperative perception under lossy communication. *IEEE Transactions on Intelligent Vehicles*, 8(4):2650–2660, 2023. 1, 3, 6
- [17] Yifan Lu, Quanhao Li, Baoan Liu, Mehrdad Dianati, Chen Feng, Siheng Chen, and Yanfeng Wang. Robust collaborative 3d object detection in presence of pose errors. In *2023 IEEE International Conference on Robotics and Automation (ICRA)*, pages 4812–4818. IEEE, 2023. 2, 3, 5, 6, 8
- [18] Cong Ma, Lei Qiao, Chengkai Zhu, Kai Liu, Zelong Kong, Qing Li, Xueqi Zhou, Yuheng Kan, and Wei Wu. Holovic: large-scale dataset and benchmark for multi-sensor holographic intersection and vehicle-infrastructure cooperative. *2024 IEEE/CVF Conference on Computer Vision and Pattern Recognition (CVPR)*, pages 22129–22138, 2024. 8
- [19] Xu Runsheng, Zhengzhong Tu Tu, Hao Xiang, Wei Shao, Bolei Zhou, and Jiaqi Ma. Cobevt: Cooperative bird’s eye view semantic segmentation with sparse transformers. In *Conference on Robot Learning (CoRL)*, 2022. 1, 6
- [20] Shaoshuai Shi, Chaoxu Guo, Li Jiang, Zhe Wang, Jianping Shi, Xiaogang Wang, and Hongsheng Li. Pv-rnn: Point-voxel feature set abstraction for 3d object detection. *2020 IEEE/CVF Conference on Computer Vision and Pattern Recognition (CVPR)*, pages 10526–10535, 2019. 2
- [21] Shaoshuai Shi, Chaoxu Guo, Li Jiang, Zhe Wang, Jianping Shi, Xiaogang Wang, and Hongsheng Li. PV-RCNN: Point-voxel feature set abstraction for 3d object detection. *2020 IEEE/CVF Conference on Computer Vision and Pattern Recognition (CVPR)*, pages 10526–10535, 2019. 3
- [22] Rui Song, Chenwei Liang, Hu Cao, Zhiran Yan, Walter Zimmer, Markus Gross, Andreas Festag, and Alois Knoll. Collaborative semantic occupancy prediction with hybrid feature fusion in connected automated vehicles. In *2024 IEEE/CVF International Conference on Computer Vision and Pattern Recognition (CVPR)*. IEEE/CVF, 2024. 1
- [23] Shihao Wang, Ying-Hao Liu, Tiancai Wang, Ying Li, and Xiangyu Zhang. Exploring object-centric temporal modeling for efficient multi-view 3d object detection. *2023 IEEE/CVF International Conference on Computer Vision (ICCV)*, pages 3598–3608, 2023. 2
- [24] Tsun-Hsuan Wang, Sivabalan Manivasagam, Ming Liang, Bin Yang, Wenyuan Zeng, and Raquel Urtasun. *V2VNet: Vehicle-to-Vehicle Communication for Joint Perception and Prediction*, page 605–621. Springer International Publishing, Cham, 2020. 1, 2, 3, 6
- [25] Yan Xia, Yusheng Xu, Shuang Li, Rui Wang, Juan Du, Daniel Cremers, and Uwe Stilla. Soe-net: A self-attention and orientation encoding network for point cloud based place

- recognition. In *Proceedings of the IEEE/CVF Conference on computer vision and pattern recognition*, pages 11348–11357, 2021. 3
- [26] Yan Xia, Mariia Gladkova, Rui Wang, Qianyun Li, Uwe Stilla, João F Henriques, and Daniel Cremers. Casspr: Cross attention single scan place recognition. In *Proceedings of the IEEE/CVF International Conference on Computer Vision (ICCV)*, pages 8461–8472, 2023. 3
- [27] Li Xiang, Junbo Yin, Wei Li, Cheng-Zhong Xu, Ruigang Yang, and Jianbing Shen. DI-V2X: Learning domain-invariant representation for vehicle-infrastructure collaborative 3d object detection. *AAAI*, 2024. 6
- [28] Runsheng Xu, Hao Xiang, Zhengzhong Tu, Xin Xia, Ming-Hsuan Yang, and Jiaqi Ma. V2x-vit: Vehicle-to-everything cooperative perception with vision transformer. In *Computer Vision – ECCV 2022*, page 107–124, Cham, 2022. Springer Nature Switzerland. 1, 2, 6
- [29] Runsheng Xu, Hao Xiang, Xin Xia, Xu Han, Jinlong Li, and Jiaqi Ma. Opv2v: An open benchmark dataset and fusion pipeline for perception with vehicle-to-vehicle communication. *2022 International Conference on Robotics and Automation (ICRA)*, page 2583–2589, 2022. 1, 2, 3, 5, 6
- [30] Runsheng Xu, Xin Xia, Jinlong Li, Hanzhao Li, Shuo Zhang, Zhengzhong Tu, Zonglin Meng, Hao Xiang, Xiaoyu Dong, Rui Song, Hongkai Yu, Bolei Zhou, and Jiaqi Ma. V2v4real: A real-world large-scale dataset for vehicle-to-vehicle cooperative perception. In *2023 IEEE/CVF Conference on Computer Vision and Pattern Recognition (CVPR)*, page 13712–13722, Vancouver, BC, Canada, 2023. IEEE. 1, 2
- [31] Yan Yan, Yuxing Mao, and Bo Li. Second: Sparsely embedded convolutional detection. *Sensors (Basel, Switzerland)*, 18, 2018. 3, 7
- [32] Binh Yang, Wenjie Luo, and Raquel Urtasun. Pixor: Real-time 3d object detection from point clouds. *2018 IEEE/CVF Conference on Computer Vision and Pattern Recognition*, pages 7652–7660, 2018. 3
- [33] Hongbo Yin, Daxin Tian, Chunmian Lin, Xuting Duan, Jianshan Zhou, Dezong Zhao, and Dongpu Cao. V2VFormer ++: Multi-modal vehicle-to-vehicle cooperative perception via global-local transformer. *IEEE Transactions on Intelligent Transportation Systems*, page 1–14, 2023. 1, 2, 3
- [34] Hongbo Yin, Daxin Tian, Chunmian Lin, Xuting Duan, Jianshan Zhou, Dezong Zhao, and Dongpu Cao. V2vformer++: Multi-modal vehicle-to-vehicle cooperative perception via global-local transformer. *IEEE Transactions on Intelligent Transportation Systems*, 25:2153–2166, 2024. 6
- [35] Haibao Yu, Yizhen Luo, Mao Shu, Yiyi Huo, Zebang Yang, Yifeng Shi, Zhenglong Guo, Hanyu Li, Xing Hu, Jirui Yuan, and Zaiqing Nie. Dair-v2x: A large-scale dataset for vehicle-infrastructure cooperative 3d object detection. In *2022 IEEE/CVF Conference on Computer Vision and Pattern Recognition (CVPR)*, page 21329–21338, New Orleans, LA, USA, 2022. IEEE. 1, 5
- [36] Haibao Yu, Yingjuan Tang, Enze Xie, Jilei Mao, Ping Luo, and Zaiqing Nie. Flow-based feature fusion for vehicle-infrastructure cooperative 3d object detection. In *Advances in Neural Information Processing Systems*, 2023. 3
- [37] Haibao Yu, Wenxian Yang, Hongzhi Ruan, Zhenwei Yang, Yingjuan Tang, Xu Gao, Xin Hao, Yifeng Shi, Yifeng Pan, Ning Sun, Juan Song, Jirui Yuan, Ping Luo, and Zaiqing Nie. V2x-seq: A large-scale sequential dataset for vehicle-infrastructure cooperative perception and forecasting. In *2023 IEEE/CVF Conference on Computer Vision and Pattern Recognition (CVPR)*, page 5486–5495, Vancouver, BC, Canada, 2023. IEEE. 2, 3
- [38] Yunshuang Yuan and Monika Sester. COMAP: A synthetic dataset for collective multi-agent perception of autonomous driving. *The International Archives of the Photogrammetry, Remote Sensing and Spatial Information Sciences*, XLIII-B2-2021:255–263, 2021. 2
- [39] Yunshuang Yuan and Monika Sester. Leveraging dynamic objects for relative localization correction in a connected autonomous vehicle network. *ISPRS Annals of the Photogrammetry, Remote Sensing and Spatial Information Sciences*, V-1-2022:101–109, 2022. 2
- [40] Yunshuang Yuan and Monika Sester. Streamlts: Query-based temporal-spatial lidar fusion for cooperative object detection, 2024. 2, 3, 4, 5, 6, 7, 8
- [41] Yunshuang Yuan, Hao Cheng, and Monika Sester. Keypoints-based deep feature fusion for cooperative vehicle detection of autonomous driving. *IEEE Robotics and Automation Letters*, 7(2):3054–3061, 2022. 1, 2, 3, 6
- [42] Yunshuang Yuan, Hao Cheng, Michael Ying Yang, and Monika Sester. Generating evidential bev maps in continuous driving space. *ISPRS Journal of Photogrammetry and Remote Sensing*, 204:27–41, 2023. 1, 2, 3, 5
- [43] Wu Zheng, Weiliang Tang, Sijin Chen, Li Jiang, and Chi-Wing Fu. CIA-SSD: Confident iou-aware single-stage object detector from point cloud. In *AAAI*, 2021. 3, 6
- [44] Yin Zhou and Oncel Tuzel. Voxnet: End-to-end learning for point cloud based 3d object detection. *2018 IEEE/CVF Conference on Computer Vision and Pattern Recognition*, pages 4490–4499, 2017. 3
- [45] Walter Zimmer, Christian Creß, Huu Tung Nguyen, and Alois C Knoll. Tumtraf intersection dataset: All you need for urban 3d camera-lidar roadside perception [best student paper award]. In *2023 IEEE Intelligent Transportation Systems ITSC*. IEEE, 2023. 8

SparseAlign: A Fully Sparse Framework for Cooperative Object Detection

Supplementary Material

A. Qualitative results

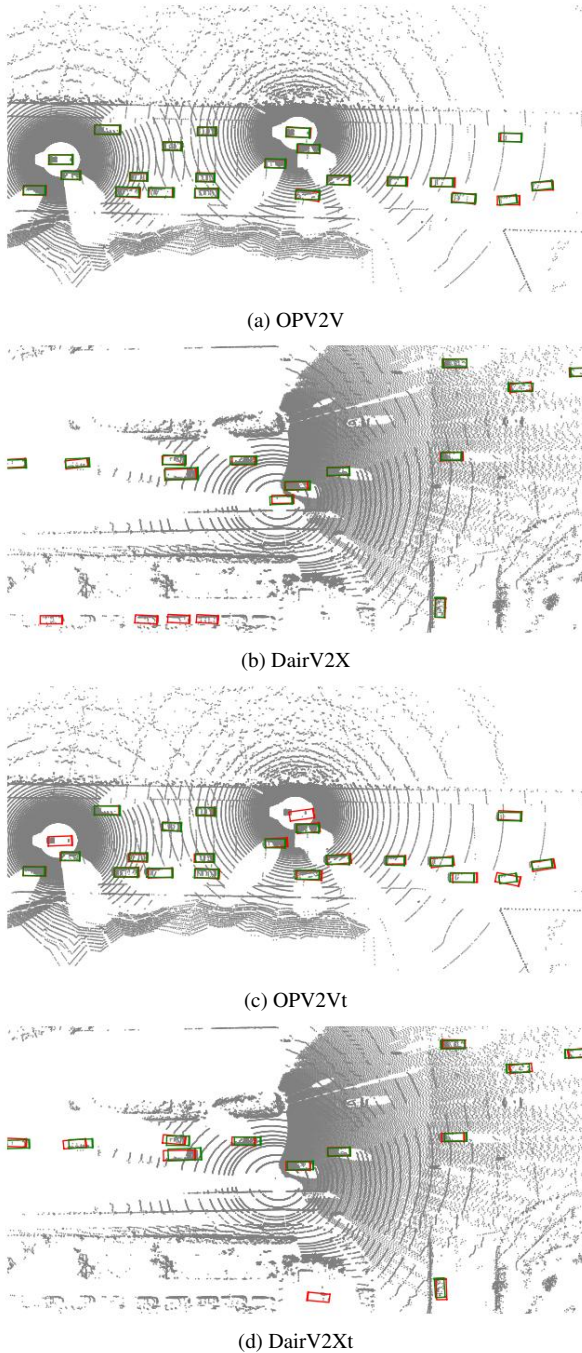


Figure 7. Qualitative results of COOD and TA-COOD. GT: green BBox, detection: red BBox.

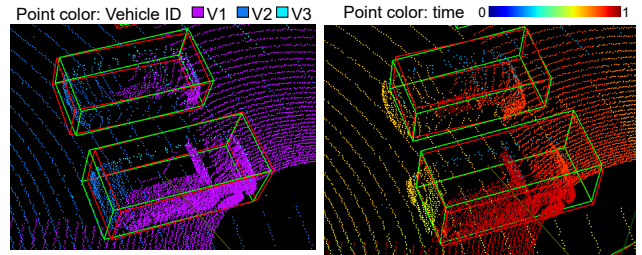


Figure 8. Qualitative result COOD (left) vs. TA-COOD (right).

Figure 7 presents qualitative results for a sample frame from each dataset. The COOD results in Figs. 7a and 7b demonstrate that our framework, SparseAlign, successfully detects most vehicles with high overlap with the ground truth. In contrast, TA-COOD poses a greater challenge, leading to less accurate detections, as shown in Figs. 7c and 7d. However, the model performs better on OPV2Vt than on DairV2Xt. We attribute this to OPV2Vt being a simulated dataset with more precise ground truth, enabling more accurate learning of fine-grained temporal context.

Figure 8 illustrates the differences between COOD and TA-COOD. On the left, point clouds scanned by three IAs are visualized in different colors. The ground truth BBoxes (green) are perfectly aligned with the synchronized scanned points, allowing the model to focus solely on learning the geometric structure of the point clouds for accurate vehicle detection. However, in TA-COOD, a more realistic setting, LiDAR points are typically scanned at different time points rather than being synchronized. In the right image, these asynchronous points are color-coded from blue (earlier scans) to red (later scans). Additionally, the ground truth bounding boxes are aligned to a future time frame rather than the exact geometry of the scanned points. This ground truth encourages the model to leverage temporal context to accurately predict vehicle positions in the near future, compensating for location errors caused by communication latency.

B. Free Space Augmentation (FSA)

Free space augmentation (FSA) was first introduced in [42] for BEV map-view semantic segmentation. Typically, point cloud data only capture reflections from obstacle surfaces. For example, in Fig. 9, points A and B represent reflections from the ground surface. With only these measurements, we can confirm the presence of obstacles at these locations but have no information about the space between them. However, distinguishing between empty and unknown spaces is crucial in many applications. For instance, autonomous vehicles can safely navigate through known empty spaces but

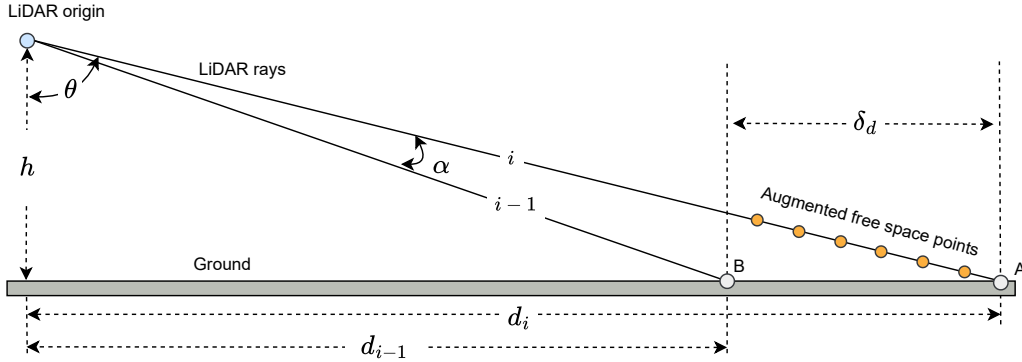


Figure 9. Free space augmentation.

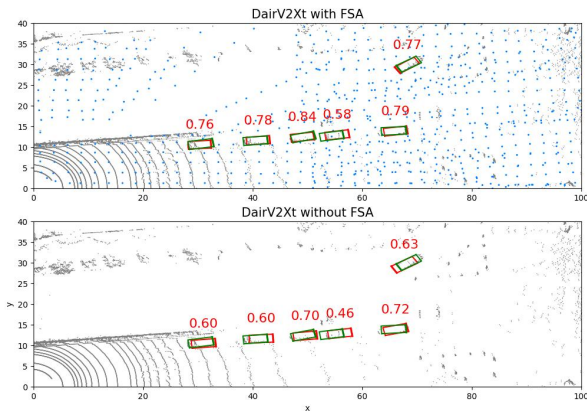


Figure 10. SparseAlign performance with and without FSA. The FSA points are in blue. Red texts are IoUs between the detected (red) and the ground-truth (green) BBoxes.

must avoid unknown areas where no measurements exist.

Each LiDAR ray provides information not only through its reflection point but also along its entire path, which consists of free space points indicating empty space. Augmenting sparse point clouds with additional points along LiDAR rays helps fill in these gaps. However, adding points along the entire ray path would be computationally prohibitive. Instead, as illustrated by the yellow points in Fig. 9, it is sufficient to augment only the free space points between adjacent laser beams.

Mathematically, given the i -th LiDAR ray with ground distance d_i , LiDAR height relative to the ground h , and the inclination angle difference α between two adjacent rays (e.g., θ for the i -th ray), the gap distance between adjacent rays is calculated as:

$$\delta_d = d_i - d_{i-1} = d_i - h \cdot \tan\left(\arctan\frac{d_i}{h} - \alpha\right) \quad (10)$$

Within this gap distance, we evenly distribute free space points to augment the original point cloud. These points

not only convey information about empty spaces but also enhance connectivity between disjoint LiDAR scan rings. This, in turn, improves the convolutional layers' ability to learn spatial context over a larger receptive field.

Figure 10 compares SparseAlign's performance with and without FSA. The results show that FSA slightly improves detection accuracy. Additionally, the augmented free space points (blue) incorporate timestamps computed based on their angles in the polar coordinate system. This enhances temporal context learning, particularly in distant regions where scan observations are sparse.

C. Dilation convolution

In this paper, we demonstrated that *SUNet* effectively mitigates ICF and CFM issues by expanding the receptive field through CEC layers. One might argue that dilated convolutional layers could serve a similar purpose. To investigate this, we conducted an additional experiment, modifying the dilation size of the first convolution layer in each *SUNet* block from one to two. The results indicate that, in this case, dilated convolutions fail to effectively expand the receptive field or mitigate the ICF issue. Instead, they degrade local feature learning.

Dilation size	OPV2V		DairV2X	
	AP0.5	AP0.7	AP0.5	AP0.7
2	0.890	0.827	0.707	0.637
1	0.924	0.885	0.773	0.638

Table 7. Comparison of normal sparse convolutions and dilation convolutions

D. Gradients calculation schedule for efficient training

To optimize training efficiency, we schedule gradient calculations only for essential modules, as illustrated in Fig. 11.

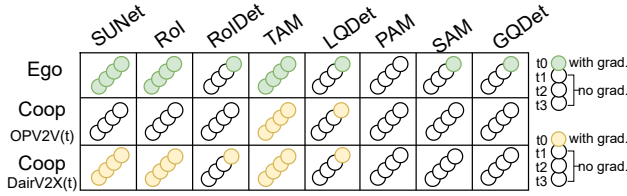


Figure 11. Schedules for gradient calculation.

t_0 is the newest frame and t_1 to t_3 is the historical frames. For the ego vehicle, we compute gradients for all modules in the latest data frame, except for *PAM*, which is trained independently. Additionally, *SUNet*, *RoI*, and *TAM* compute gradients across all frames to facilitate temporal feature learning.

In the OPV2V and OPV2Vt datasets, each IA is equipped with identical range-view sensors. Consequently, we disable gradient calculations for the first three modules in cooperative IAs, as their data exhibit the same feature patterns as those of the ego IA.

In contrast, in the DairV2X and DairV2Xt datasets, cooperative IAs are infrastructure-based, featuring different sensors and viewing angles from vehicles. To ensure effective learning from infrastructure data, gradient calculations remain enabled for *SUNet*, *RoI*, and *TAM* in cooperative agents.

The final two modules pertain to the fusion process, which occurs exclusively in the ego vehicle. Therefore, no gradient calculations are performed on the cooperative side. Notably, we enable gradients for only one cooperative IA when necessary, irrespective of the total number of IAs.

E. Average precision on 3D metric

	TransIFF[4]	SparseAlign
OPV2V	-	0.922/0.816
DairV2X	0.596/0.460	0.727/0.352
OPV2Vt	-	0.898/0.703
DairV2Xt	-	0.698/0.237

Table 8. AP 3D at IoU thresholds of 0.5/0.7.

In the paper, we used BEV IoU thresholds to calculate the average precision. Here, we also report results based on 3D IoU thresholds for convenient comparison with other methods that use 3D AP as an evaluation metric, such as TransIFF[4]. The results in Tab. 8 indicate that our SparseAlign achieves higher AP at a 3D IoU threshold of 0.5 but lower AP at 0.7. We attribute this to the fact that the three alignment modules in SparseAlign consider only the x and y coordinates in geometric operations during the fusion process, without explicitly accounting for the z -axis.

SparseAlign: A Fully Sparse Framework for Cooperative Object Detection (Rebuttal)

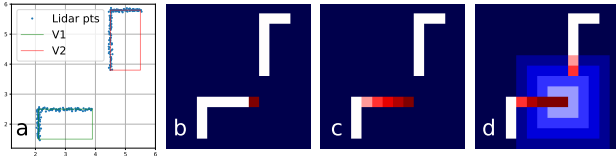


Figure 1. Receptive field (RF) after 4 sparse convolutions (convs). a. Lidar points; b. Spare pixels (white) with a conv center point (red); c. RF coverage of 4 normal sparse convs (red); d. RF coverage of 4 CECs (red+light blue, darkest blue is background).

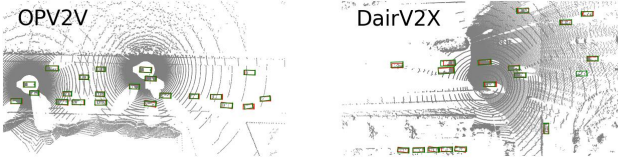


Figure 2. Qualitative result COOD. GT: green, detection: red

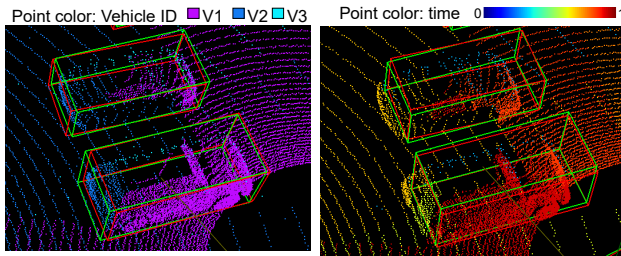


Figure 3. Qualitative result COOD (left) vs. TA-COOD (right).

	OPV2V AP0.5/0.7	DairV2X AP0.5/0.7
No SAM	0.847/0.756	0.671/0.528
QUEST spatial fusion	0.888/0.869	0.749/0.622
late fusion	0.857/0.835	0.767/0.612

Table 1. Results of Late fusion and ablation on SAM and QUEST.

We thank the reviewers (R1:PvGq, R2:avR7, R3:ucwb) for the positive and constructive feedback. We are encouraged they found our model is "efficient" and has "solid technical advancement", the experiments are "extensive", the performance gain is "significant" and "exceptional", and "offering a new direction for cooperative perception tasks". We also appreciate the suggestions on writing clarity and will make corresponding improvements, along with **releasing the code** for better reproducibility in the final version.

R1.1: Activity level. The integration of V2X for safer and more efficient mobility is a strategic plan of government agencies (e.g. US: DOT JPO, NHTSA; EU: C-ITS). The citations of OPV2V: **388** and DairV2X: **358** within two years demonstrate that COOD is active. Fewer recent comparative works are due to the lack of code and inconsistency of evaluation metrics in these works. For this concern, here we add more results of recent TransIFF (ICCV2023) and QUEST (ICRA2024) for comparison (see R3.2).

R1.2: Training time. About 35 hours on a single RTX 4090 GPU and an Intel i7-8700 CPU.

R1.3-4: CompassRose as an auxiliary contribution; Focal loss for classification (fore- vs. background), Smooth-L1

for regression ($\mathcal{B}_{dir}, \mathcal{B}_{scr}, dx, dy, dz, l, w, h$). Due to space limitation, we discuss them in depth in the final version.

R1.5: Qualitative results. The results of COOD and TA-COOD in a holistic view are similar, we show one example in Figure 2 and a comparison in Figure 3. The GTs (green boxes) of TA-COOD are not aligned with the vehicle points (orange latency points are outside the boxes, see R2.6).

R2.1: ICF,CFM. ICF: the receptive field (RF) of sparse convolutions. Figure 1.c: RF of normal convs over V1 points does not cover V2 points; hence V1 and V2 points are isolated. Figure 1.d: CECs solve ICF and CFM.

R2.2: Symbol relation. c and e should be in the superscript as defined in line 229. (x, y) are transformed with $[x^e, y^e]^T = R \cdot [x^c, y^c]^T$, R : rotation matrix (coop. to ego).

R2.3: Uncertainty. We only use $LQDet$ detection confidences during testing to filter the queries (see Sec. 5.5).

R2.4: V2VAM. For consistency, we report the results from the official OPV2V repository. All comparative methods are on single-frame and use dense operations on BEV maps, which can hardly be extended to multi-frames on GTX4090. This also reflects the efficiency of our *SparseAlign*.

R2.5: TA-COOD. LiDAR points are captured sequentially over time (main paper Fig. 2, TAM). COOD GT BBoxes (dashed lines) align with LiDAR points; TA-COOD GT BBoxes (solid lines) align with a global timestamp t_g , requiring the model to accurately predict the BBox location at t_g . COOD predicts locations solely based on point cloud geometry, TA-COOD incorporates temporal context for accurate prediction at t_g , and also enables *SparseAlign* to handle location errors due to communication latency.

R2.6: FSA. is from [39] but not commonly used in previous works; as suggested, we shortly discuss it in Sec. 3 Method.

R2.7: Late-fusion. We focus on and compare only intermediate fusion methods. For your concern, late fusion, which only shares BBoxes (CPM size $< 3KB$, about 3% of the query feature size), demonstrates worse performance (see Table 1; discussion will be added to Sec. 5.5).

R3.1: CEC. The reason for using CEC is shortly discussed in Sec. 1 (Main paper). Figure 1 is an additional illustration. See R2.1: ICF,CFM for more details.

R3.2: TransIFF, QUEST. TransIFF 3D AP.5/0.7: 0.596/0.46 will be in sup. material, instead of Tab. 2 (Main paper) that uses BEV AP. Our 3D AP.5:0.727 is higher than TransIFF. However, AP.7:0.352 is worse as we only use x, y in the 3 alignment modules. QUEST spatial fusion result is in Table 1. We will add the detailed analysis in the final version.

R3.3: PAM,SAM. PAM ablation is discussed in Sec. 5.4 and Fig. 5 (Main paper). Ablation on SAM: see Table 1.

R3.4: PAM improvement. The CoAlign pose-align in Fig. 5 (Main paper) is location-based and has no learning modules.

R3: Roadside benchmarks. will be added to future work.